ROYAL SOCIETY OF CHEMISTRY

PAPER

Construction of a self-supporting Ni$_2$P–WO$_3$ heterostructure for highly efficient hydrogen evolution under both caustic and acidic conditions†

Benzhi Wang,‡[a] Lixia Wang,‡[a] Yongteng Qian, [c] Yuting Yang, [a] Tayirjan Taylor Isimjan*[b] and Xiulin Yang*[a]

The development of low-cost and highly efficient hydrogen evolution reaction (HER) catalysts remains a significant challenge for the advancement of sustainable energy conversion systems. Herein, we have reported the successful preparation of an amorphous WO$_3$ adjusted nickel phosphide (Ni$_2$P–WO$_3$/CC)-based HER catalyst through a facile and scalable method. The optimized Ni$_2$P–WO$_3$/CC catalyst has excellent HER performance under both 1.0 M KOH (105 mV@10 mA cm^{-2}) and 0.5 M H$_2$SO$_4$ (107 mV@10 mA cm^{-2}) conditions, respectively. Moreover, in a simulated industrial two-electrode alkaline system, the developed catalyst can provide current densities of 500 and 1000 mA cm^{-2} at cell voltages of 1.8 and 1.9 V, respectively. Such excellent HER activity is significantly higher than those of noble-metal-based catalysts. These results indicate that WO$_3$ has an important role in inducing the transformation of the nickel phosphide crystal structure. The remarkable catalytic performance is due to the synergy between WO$_3$ and Ni$_2$P, as well as the unique porous structure, which can enhance electron transfer, supply more active sites, and accelerate electrolyte transfer and gas emission. This study facilitates the development of new design strategies for HER catalysts and the promotion of their industrial applications.

Introduction

Finding renewable energy sources to replace increasingly depleted fossil fuels is a key challenge facing humanity in the 21st century.[1–3] As an abundant and efficient energy carrier with broad application prospects, hydrogen is an ideal choice to replace fossil fuels.[4–7] Hydrogen production from water electrolysis is an important source without pollution or greenhouse gas emissions.[8–11] Around 44.5 million tons of hydrogen are generated annually from various sources; only 4% is produced from water electrolysis and the rest is from steam methane reforming and coal gasification.[12] This is because it is difficult to find suitable water splitting catalysts. At present, platinum-based catalysts are still the most effective hydrogen evolution catalysts.[3,13] However, the high cost and limited Pt reserves limit their practical application. Thus, alternative materials must be urgently developed.

Recently, transition metal phosphides (TMPs) have proved to be a new type of catalyst with great development prospects due to their excellent physical and chemical properties.[14–16] Moreover, compared with metal oxides and metal sulfides, the P atom is considered as a good proton acceptor compared to S and O atoms, and hence, TMPs have become the most promising HER catalysts and are also considered as potential substitutes for Pt.[17,18] Among the many transition metal ions, Markovic and co-workers confirmed that Ni active species enhance water dissociation kinetics to generate atomic H that needs to be combined on the active site to form H$_2$ molecules.[19] Therefore, various combinations of Ni and P have been widely investigated for the development of high efficiency HER catalysts.[20–23] However, the synthesis of nickel phosphide-based electrocatalysts with high HER activity still has challenges, such as harsh reaction conditions, expensive equipment and complicated processes.[18,24] These disadvantages greatly limit their wide application. Most recently, many reports have highlighted tungsten oxide (WO$_X$) as an excellent co-catalyst because

[a]Guangxi Key Laboratory of Low Carbon Energy Materials, School of Chemistry and Pharmaceutical Sciences, Guangxi Normal University, Guilin 541004, China. E-mail: xlyang@gxnu.edu.cn

[b]Saudi Arabia Basic Industries Corporation (SABIC) at King Abdullah University of Science and Technology (KAUST), Thuwal 23955-6900, Saudi Arabia. E-mail: isimjant@sabic.com

[c]Department of Physics, Interdisciplinary Course of Physics and Chemistry, Sungkyunkwan University, 2066, Seobu-ro, Jangan-gu, Suwon, Gyeonggi-do 16419, Republic of Korea

‡ These authors contributed equally.

its thermodynamic stability in acidic solutions is much higher than that of most metal oxides. At the same time, the conductivity of tungsten oxide (10–20 S cm^{-1}) is higher than that of 1T-WS$_2$ (7 S cm^{-1}).[25,26] For example, Jin *et al.* observed that amorphous tungsten-doped nickel phosphide (α-WNP) microspheres with ravine-like nanostructures require 110 mV overpotential at 20 mA cm^{-2}.[27] However, the poor catalytic performance, low current density and difficulty in large-scale preparation greatly limit their practical applications.[28] In addition, it is still a very challenging task to combine phosphides with various excellent properties and thermodynamically stable tungsten oxide in the hydrogen evolution reaction.

Herein, we constructed a novel catalyst having heterostructures containing Ni$_5$P$_4$, Ni$_2$P$_4$O$_{12}$–WO$_3$, and Ni$_2$P–WO$_3$ by controlling the introduction of amorphous W oxide. Scanning electron microscopy (SEM, Quanta FEG 200, Holland) and X-ray diffractometry (XRD, D/Max 2500 V PC system with Cu Kα radiation, Rigaku, Japan) analyses showed that the morphology and crystal structure of the prepared catalyst changed with the introduction of WO$_3$. X-ray photoelectron spectroscopy (XPS, JPS-9010 TR Photoelectron Spectrometer, Japan) indicated that the introduction of amorphous WO$_3$ enhances the electronic interaction between Ni and P. Electrochemical experiments showed that the optimized Ni$_2$P–WO$_3$ exhibits excellent hydrogen evolution performance under acidic and alkaline conditions, with a low overpotential, small Tafel slope, and long-term durability. In addition, the two-electrode system composed of Ni$_2$P–WO$_3$ and RuO$_2$ in 30% KOH solution requires cell voltages of only 1.8 and 1.9 V to achieve current densities of 500 and 1000 mA cm^{-2}, respectively. Its performance is higher than that of a two-electrode system composed of RuO$_2$ and commercial Pt/C, which proves that the as-prepared catalyst has excellent prospects for commercial applications.

Experimental

Preparation of Ni–W-species/CC by stepwise electrodeposition

The specific steps for the purification of carbon cloth (CC, 1 cm × 1.5 cm) are as follows: ultrasonic cleaning of CC with H$_2$SO$_4$, H$_2$O and ethanol sequentially for 5 min respectively, and then cycling three times. Then, the purified CC was employed as the working electrode and electrodeposited in Ni(NO$_3$)$_2$ solution at −10 mA cm^{-2} for 1.0 h to prepare Ni-species/CC. After rinsing with abundant water and natural drying, Ni-species/CC was used as a working electrode again for electrodeposition for 10, 30, 60, and 90 min at −10 mA cm^{-2} in 0.1 M (NH$_4$)$_{10}$H$_2$(W$_2$O$_7$)$_6$. The maximum W content was achieved at 30 min, and then the W content started to decrease with the increase of time indicating that the dissociation dominates in the later stage of the electrochemical process. We reported a similar result in our earlier work.[29] The electrodeposited products are named as Ni–W-species/CC-10, Ni–W-species/CC-30, Ni–W-species/CC-60, and Ni–W-species/CC-90, respectively.

Synthesis of Ni$_5$P$_4$/CC, WO$_3$/CC, and Ni$_2$P–WO$_3$/CC

The phosphating process was carried out in a tube furnace. The white NaH$_2$PO$_2$ powder is placed upstream of the quartz tube as the precursor of PH$_3$ gas in a ceramic boat, and the phosphating samples are placed downstream in another ceramic boat. The temperature of the tube furnace is increased to 350 °C at a rate of 5 °C min^{-1} in an Ar atmosphere (20 sccm). After being kept at a constant temperature for 2 h, it is cooled naturally to room temperature. Then, a series of products were prepared and identified as Ni$_2$P–WO$_3$/CC-10, Ni$_2$P–WO$_3$/CC-30, Ni$_2$P–WO$_3$/CC-60, and Ni$_2$P–WO$_3$/CC-90. By comparison, commercial Pt/C-modified CC was fabricated. In brief, the commercial Pt/C (5.0 mg) was ultrasonically dispersed in 0.5 mL of 0.2 wt% Nafion solution for 30 min. Then, the resulting mixture was pipetted onto the surface of CC (1 cm^2) and dried naturally in air.

Ni$_5$P$_4$/CC was prepared by electro-deposition of Ni metal on CC followed by a similar phosphating approach to that described above. However, WO$_3$/CC was prepared by the drop-casting method whereas certain drops of 1.0 M (NH$_4$)$_{10}$H$_2$(W$_2$O$_7$)$_6$ were placed on the surface of the CC, and dried naturally. The objective of preparing Ni$_5$P$_4$/CC and WO$_3$/CC is to investigate the contributions of Ni and W towards the activity of Ni$_2$P–WO$_3$/CC while highlighting the significance of the synergy between the two species.

Synthesis of Ni$_2$P/CC

The synthesis of Ni$_2$P nanoparticles was based on a previously reported method.[30] Briefly, 0.66 g of NaH$_2$PO$_2$ and 0.3 g of NiCl$_2$·6H$_2$O were mixed and ground together at room temperature. The resulting solid was placed in a quartz boat and transferred into a tubular furnace. The temperature of the tube furnace was increased to 250 °C with a heating rate of 5 °C min^{-1} and maintained for 1.0 hour under a constant flow of N$_2$. The color of the solid mixture changed from green/white to black during the heating process. The resulting solid was then cooled to ambient temperature. The black solid was collected and ground. Side products and impurities were washed off using distilled water. The nanoparticles were dried overnight in an oven at 50 °C. The Ni$_2$P modified CC electrode (Ni$_2$P/CC) was prepared by ultrasonic dispersion of Ni$_2$P particles (10.0 mg) in 0.5 mL of 0.2 wt% Nafion solution for 30 min, and then pipetting the resulting slurry onto the surface of CC (1 cm^2) and drying it naturally in air. The material characterization and the electrochemical measurements are shown in the ESI.†

Electrochemical measurements

The electrochemical performance of the as-prepared catalysts was investigated using an electrochemical workstation (Biologic VMP3) with a typical three-electrode system in a 1.0 M KOH electrolyte. The catalyst modified carbon cloth, a graphite plate, and a saturated calomel electrode (SCE) were used as working, counter, and reference electrodes, respectively. The loading of Ni$_2$P–WO$_3$ on CC is approximately 11.82 mg cm^{-2}. CV tests were carried out for approximately five cycles to stabilize the electrocatalytic performance of the catalyst at a scan rate of 20 mV s^{-1}. Subsequently, linear sweep voltammetry (LSV) curves were obtained at a low scan rate of 0.5 mV s^{-1}, and electrochemical impedance spectroscopy (EIS) was performed near the onset potential over the frequency range from 200 kHz to 10 MHz. All

potentials (*vs.* SCE) in this work were calibrated to the reversible hydrogen electrode (RHE) using the average CV curves of the two potentials at which the current crossed zero (1.040 V). This value was considered to be the thermodynamic potential in H_2-saturated 1.0 M KOH (Fig. S1†). All reported curves were corrected by *iR* compensation, and all electrochemical tests were performed at room temperature (25 ± 1 °C).

Results and discussion

The schematic diagram of the preparation of the $Ni_2P–WO_3/CC$ composite is shown in Fig. 1a. The synthesis process is combining an *in situ* electrodeposition process with a phosphating treatment.

XRD analysis was conducted to study the crystal phase of the product. Fig. 1b and c show the diffraction peaks and standard spectra after the electrodeposition of W species for different times using Ni-species/CC as electrodes and after the phosphating treatment. The crystal structure after the phosphating treatment without the electrodeposition of W species is consistent with the Ni_5P_4 standard (JCPDS: 18-0883). When the W electrodeposition time was 10 min, the crystal structure corresponded to the $Ni_2P_4O_{12}$ (JCPDS: 76-1557) and Ni_2P standards (JCPDS: 74-1385). When the W electrodeposition time was >30 min, the crystal structure was in good agreement with the Ni_2P standard. However, we are not able to find corresponding components that match with all the peaks. Therefore, we used the majority peaks to find the closest structure possible that is pointing towards Ni_2P. The two distinctive peaks of Ni_2P at 40.7° and 44.6° correspond to (111) and (201) crystal planes,

respectively, and they were also confirmed by TEM (Fig. 2c). Interestingly, the change in peak intensity is presumably due to the strong interaction between the W and Ni components. Moreover, a new peak that appeared at 52° could be the indication of surface oxidation that may belong to (332) of $Ni_2P_4O_{12}$. It is worth noting that the diffraction peak of tungsten oxide is not detectable in $Ni_2P–WO_3/CC$, indicating that the tungsten oxide content in the composite is low or exists in an amorphous form. As a control, the synthesized N_2P particles and WO_3/CC control samples are basically consistent with the crystal diffraction peaks of their standard samples (Fig. 1c and S2†), indicating that the target control materials have been synthesized for the next study. Among them, synthesized N_2P powder showed an irregular particle shape with obvious agglomeration (Fig. S3†). Especially it was noted that when electroplating the precursor of W on CC was attempted, almost no tungsten species was detected, indicating that electroplating the Ni species first is a prerequisite for the construction of Ni–W composites.

The material morphology and microstructure were studied by SEM and TEM. The SEM image shows that the $Ni_2P–WO_3$ composite with a needle-like structure on the surface grew vertically and uniformly on the carbon tube and formed a porous structure (Fig. 2a). This porous structure promotes mass transfer and formation of many reaction sites, which improve the electrochemical activity. The morphology of the material changes with the W electrodeposition time (Fig. S4†). Notably, when the deposition time of the W component is longer than 30 min, the surface of the phosphating product has a part of needle-like (60 min) or flake-like (90 min) structure.
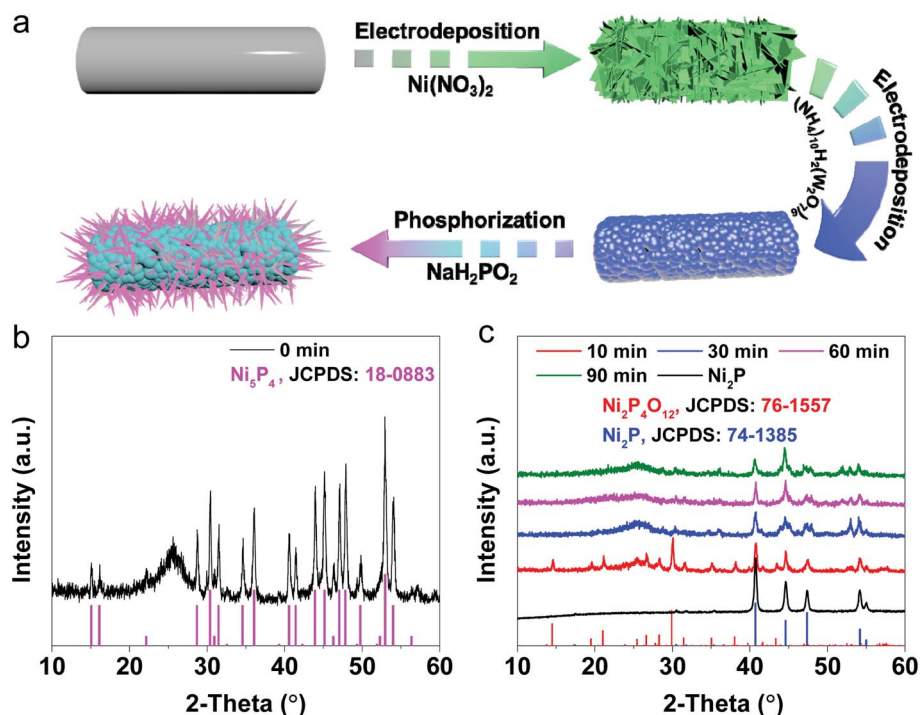
Fig. 1 (a) Schematic illustration of the synthesis of $Ni_2P–WO_3/CC$. XRD patterns of (b) nickel phosphide and (c) after electrodepositing W for different times (inset: histograms of standard Ni_5P_4, $Ni_2P_4O_{12}$ and Ni_2P).
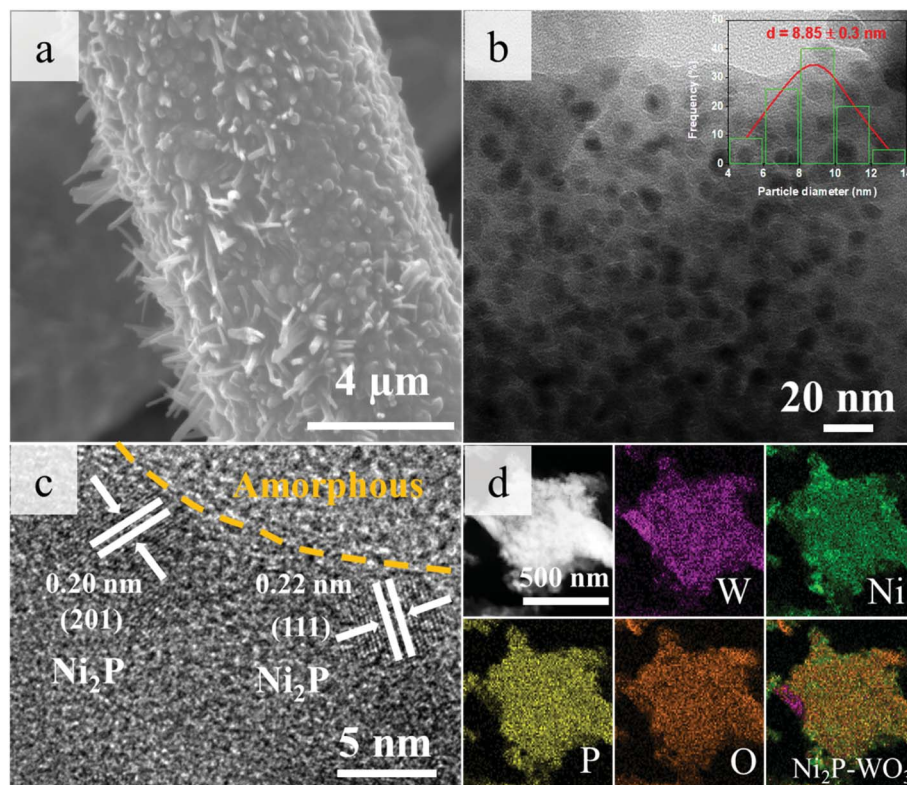
Fig. 2 (a) SEM, (b) TEM, and (c) HRTEM image of Ni_2P-WO_3/CC. (d) HAADF-TEM elemental images of Ni_2P-WO_3/CC.

These results indicated that the WO_3 species in the composite remains constant during the phosphating process, while some of the Ni species will overflow to the surface of the composite with the morphology changing from particulate to needle-like or flake-like. These findings are consistent with the gradual decrease in the mass fraction of W species detected by ICP-AES after 30 min electrodeposition (Table S1†). The TEM image reveals that the needle-shaped Ni_2P-WO_3/CC composite is composed of abundant grains (Fig. 2b), consistent with the SEM results, and particles with the average size of ~8.85 nm. The HRTEM image of the catalyst shows areas with high crystallinity and amorphous nature (Fig. 2c). The distances of the lattice fringes of ~0.20 and ~0.22 nm in the high crystallinity region are matched with the (201) and (111) crystal planes of Ni_2P,
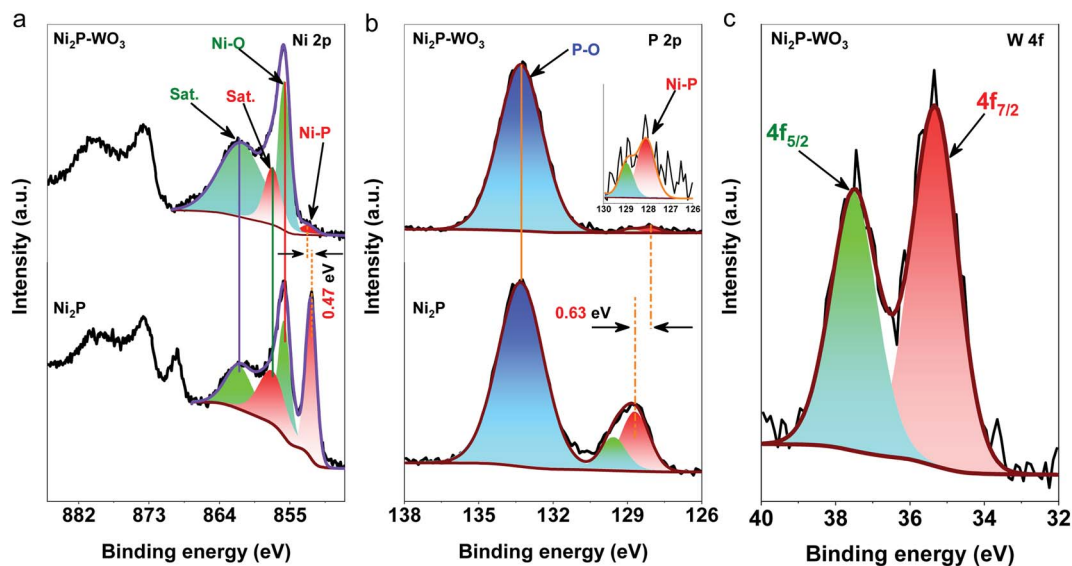
Fig. 3 XPS spectra of (a) Ni 2p, (b) P 2p, and (c) W 4f regions from Ni_2P-WO_3 and Ni_2P.

respectively.[31,32] The amorphous region is attributed to amorphous tungsten oxide. The high-angle annular dark-field (HAADF) TEM result shows that the elements of W, Ni, P and O are uniformly distributed throughout the composite (Fig. 2d), which is consistent with the assumed uniform heterostructure between Ni_2P and WO_3 species. In addition, the specific surface area and porosity of Ni_2P–WO_3-60 scraped from CC were explored using nitrogen adsorption–desorption isotherms (Fig. S5†), and the results showed that the Brunauer–Emmett–Teller (BET) specific surface area of the material was about 20 $m^2 g^{-1}$, and the average pore size was about 5 nm. The relatively high BET surface area and porosity indicate a faster mass transfer rate and a higher chance of exposing active sites, which are crucial for high catalytic performance. Inductively coupled plasma atomic emission spectrometry (ICP-AES) was conducted to analyse the mass fraction of W and Ni in the composite materials after electrodepositing W for different times. The amounts of W and Ni in the sample with the W electrodeposition time of 1.0 h, were 17.11 and 38.45 wt%, respectively, and the molar ratio of W/Ni was 1/7.04 (Table S1†).

The chemical state and elemental composition of Ni_2P–WO_3 were analysed by XPS, and the results confirmed W, Ni, O, P, and C in Ni_2P–WO_3 (Fig. S6a†). The binding energies were corrected using C 1s as the standard. The C 1s spectrum shows four peaks, including C–O (286.0 eV), C=O (288.0 eV), C=C (284.0 eV), and C–C (284.8 eV) (Fig. S6b†).[33] The Ni $2p_{3/2}$ spectra of Ni_2P–WO_3 and Ni_2P are displayed in Fig. 3a, and two distinct spin–orbit peaks and two broad satellite peaks can be observed. This demonstrates that Ni exists in two different valence states in Ni_2P–WO_3 and Ni_2P. The binding energies of Ni_2P–WO_3 at

853.08, 856.0, 857.48, and 861.54 eV are attributed to the Ni–P and Ni–O bonds and their satellite peaks.[34,35]

It is worth noting that the binding energy of Ni_2P attributed to the Ni–P bond was negatively shifted by about 0.47 eV (to 852.61 eV) compared with the position of the Ni–P bond in Ni_2P–WO_3. The high-resolution spectrum of Ni_2P–WO_3 is mainly divided into P 2p peaks corresponding to the P–O bond (133.32 eV)[36] and the P $2p_{1/2}$ (128.93 eV) and P $2p_{3/2}$ (128.06 eV) peaks ascribed to the Ni–P bond (Fig. 3b).[37] The peaks of P $2p_{3/2}$ and P $2p_{1/2}$ are matched with the 128.69 and 129.56 eV in Ni_2P, respectively, and both are positively shifted by 0.63 eV compared to corresponding signals from Ni_2P–WO_3 (shown in the inset of Fig. 3b). The shift in the peaks of P and Ni in Ni_2P–WO_3 indicates that the electrons may be transferred from Ni to P in the composite, which promotes the HER. The high-resolution W 4f spectra (Fig. 3c) are divided into W $4f_{5/2}$ (37.49 eV) and W $4f_{7/2}$ (35.32 eV) peaks corresponding to the W–O bond. These results are consistent with most previously reported binding energies of amorphous WO_3 components,[38–40] further demonstrating that W exists in the oxide form within the Ni_2P–WO_3 composite.

The electrocatalytic activity of Ni_2P–WO_3 with different W electrodeposition times and the Pt/C catalyst in an alkaline electrolyte was investigated (Fig. 4a). With an increase in the overpotential, the cathode current density of Ni_2P–WO_3 increases rapidly, which proves that Ni_2P–WO_3 has excellent HER activity. When the current density reached 10 mA cm^{-2}, the Ni_2P–WO_3-60 electrode showed an overpotential of ~105 mV, which was lower than that of any of the other Ni_2P–WO_3 samples. In addition, the catalytic performance of Ni_2P–WO_3-60 is also superior to those of Ni_2P and WO_3 catalysts under
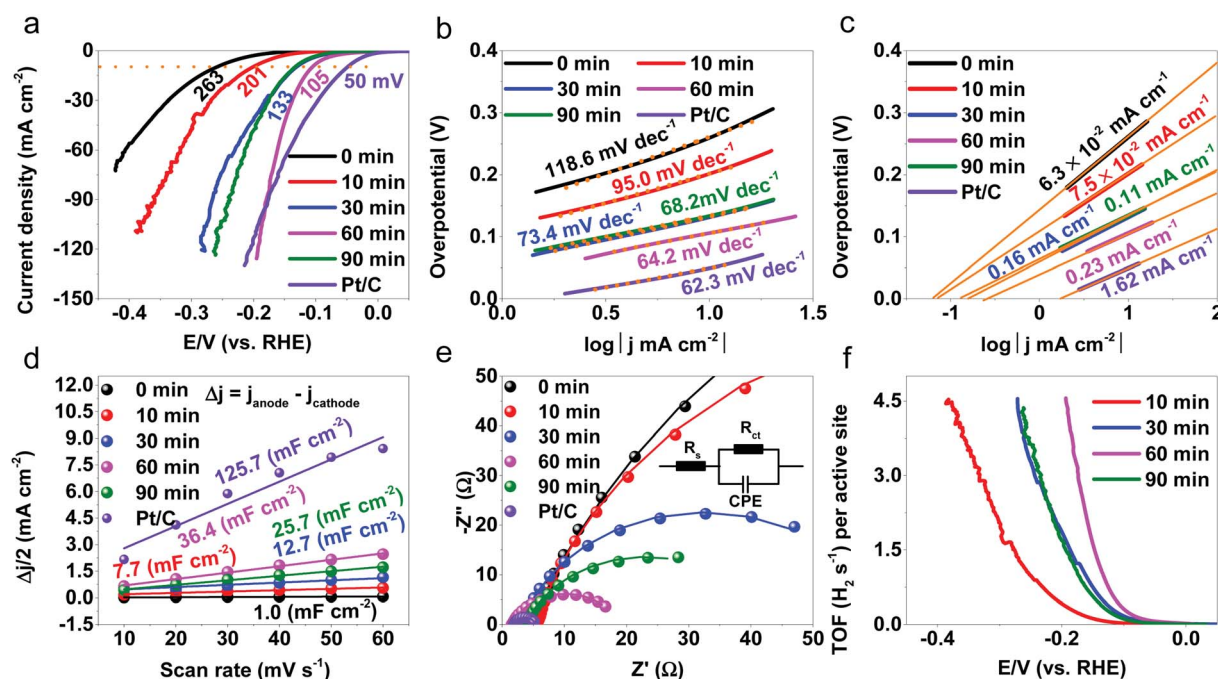
Fig. 4 (a) LSV curves of the samples, (b) Tafel slopes of the samples, (c) exchange current density of the samples, (d) C_{dl}, (e) Nyquist plots, and (f) TOF profiles versus potentials for catalysts with W electrodeposition times and 20 wt% Pt/C in 1.0 M KOH.
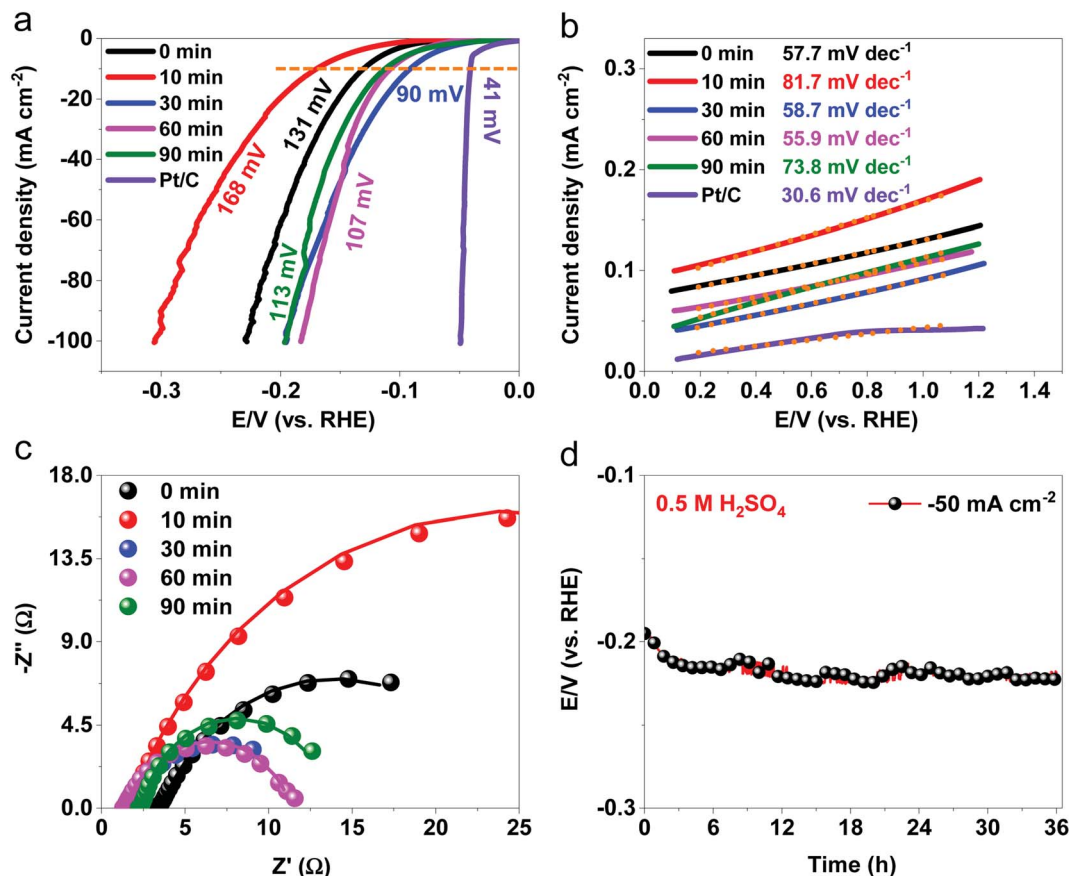
Fig. 5 (a) LSV curves of the samples, (b) Tafel slopes of the samples, (c) Nyquist plot of catalysts with different W electrodeposition times and 20 wt% Pt/C in 0.5 M H_2SO_4. (d) Durability test of $Ni_2P–WO_3$-60 at −50 mA $cm^{−2}$ in 0.5 M H_2SO_4.

alkaline and acidic conditions (Fig. S7†), as well as most of the previously reported catalysts (Table S2†). Moreover, when the overpotential reached 180 mV, the current densities (−92.0 mA $cm^{−2}$) of $Ni_2P–WO_3$-60 and commercial Pt/C catalysts are the same. It was noted that the catalytic activity of $Ni_2P–WO_3$-60 was much higher than those of noble-metal-based catalysts (Pt/C), meaning that $Ni_2P–WO_3$-60 has great potential in industrial applications. Particularly, a low overpotential of ~262 mV can be achieved at 500 mA $cm^{−2}$ in 30 wt% KOH solution, indicating its remarkable catalytic activity (Fig. S8a†).

The catalytic kinetics and rate-determining steps in the HER can usually be assessed using the Tafel slope. Fig. 4b shows that the Tafel slopes of $Ni_2P–WO_3$-0, $Ni_2P–WO_3$-10, $Ni_2P–WO_3$-30, $Ni_2P–WO_3$-60, and $Ni_2P–WO_3$-90 were at 118.6, 95.0, 73.4, 64.2, and 68.2 mV $dec^{−1}$, respectively. These results indicate that the Volmer–Heyrovsky step in alkaline solution is the rate-determining step during the HER.[41] In addition, the $Ni_2P–WO_3$-60 catalyst shows a smaller Tafel slope than other $Ni_2P–WO_3$ catalysts, meaning that the activation energy of $Ni_2P–WO_3$-60 is lower. The exchange current density (Fig. 4c) also significantly influences the electrode performance and is calculated through extrapolating the Tafel slope. As is shown, $Ni_2P–WO_3$-60 presents an exchange current density of 0.23 mA $cm^{−2}$ that is higher than those of $Ni_2P–WO_3$-0 ($6.3 \times 10^{−2}$ mA $cm^{−2}$), $Ni_2P–WO_3$-10 ($7.5 \times 10^{−2}$ mA $cm^{−2}$), $Ni_2P–WO_3$-30 (0.16 mA $cm^{−2}$), or $Ni_2P–$

WO_3-90 (0.11 mA $cm^{−2}$). This confirms that $Ni_2P–WO_3$-60 has the fastest electrode kinetics among the $Ni_2P–WO_3$ samples.[42]

The electrochemical double-layer capacitance (C_{dl}) also is a key parameter of the catalyst.[43] The C_{dl} values can be obtained by cyclic voltammetry (CV) with different scan rates in non-faradaic regions (Fig. S9†). The C_{dl} value of $Ni_2P–WO_3$-60 is 36.4 mF $cm^{−2}$ (Fig. 4d), which is much higher than those of $Ni_2P–WO_3$-0 (1.0 mF $cm^{−2}$), $Ni_2P–WO_3$-10 (7.7 mF $cm^{−2}$), $Ni_2P–WO_3$-30 (12.7 mF $cm^{−2}$), and $Ni_2P–WO_3$-90 (25.7 mF $cm^{−2}$), but it is obviously smaller than that of Pt/C (125.7 mF $cm^{−2}$). Generally, the value of C_{dl} is directly proportional to the electrochemically active surface area (ECSA) (see ESI†).[44] Therefore, if a catalyst has a larger ECSA, more active sites are available. Here, the $Ni_2P–WO_3$-60 catalyst can offer the most available catalytic active sites among all non-noble metal catalysts. To reflect the intrinsic catalytic activity, we normalized the ECSA of catalytic activity. As shown in Fig. S10,† the $Ni_2P–WO_3$-60 catalyst has excellent intrinsic hydrogen evolution activity.

At the same time, the R_{ct} of $Ni_2P–WO_3$-60 is the lowest among the $Ni_2P–WO_3$ catalysts (Fig. 4e), which indicates that the $Ni_2P–WO_3$-60 catalyst has good conductivity and can promote faster ion transfer, resulting in a remarkable HER performance.[3] The turnover frequency (TOF) is the inherent intrinsic activity of electrocatalysts and is employed to evaluate the number of H_2 molecules released per second from each active site. The TOF
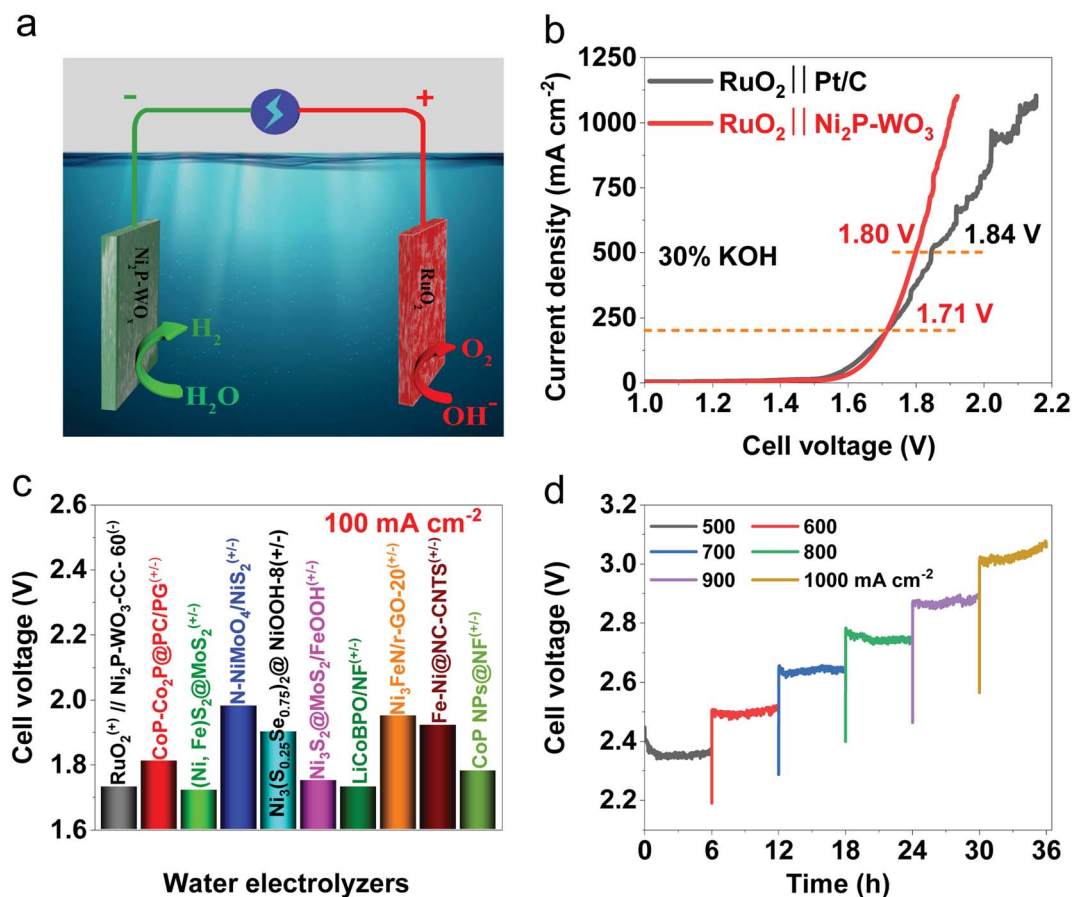
Fig. 6 (a) Schematic illustration of the water splitting cell by employing RuO_2 and $Ni_2P–WO_3$-60 as the anode and cathode, respectively. (b) Comparison of the water splitting activity of $RuO_2^{(+)}\|Ni_2P–WO_3$-60$^{(-)}$ versus $RuO_2^{(+)}\|Pt/C^{(-)}$ in 30 wt% KOH at high current. (c) Comparison of cell voltages for the currently available electrolytic cells in 1.0 M KOH at 100 mA cm^{-2}. (d) Long-term cycling tests of $Ni_2P–WO_3$-60 at different current densities in 30 wt% KOH.

value of the catalyst increases rapidly with an increase in the applied potential under alkaline conditions (Fig. 4f). This trend was the most obvious for $Ni_2P–WO_3$-60. For $Ni_2P–WO_3$-60, when the overpotential was 100 mV, the TOF value was 0.31 s^{-1}, which is higher than those of other $Ni_2P–WO_3$ catalysts. The high TOF value indicates that $Ni_2P–WO_3$-60 can effectively promote the HER and that is the inherent reason for its superior performance.[45]

The prepared $Ni_2P–WO_3$ samples under acidic conditions also show excellent HER activity. Fig. 5a shows the LSV result of the catalysts with different W electrodeposition times and 20 wt% Pt/C in acid electrolyte. The overpotentials of the prepared $Ni_2P–WO_3$-0, $Ni_2P–WO_3$-10, $Ni_2P–WO_3$-30, $Ni_2P–WO_3$-60, $Ni_2P–WO_3$-90, and commercial Pt/C were 131, 168, 90, 107, 113, and 41 mV at −10 mA cm^{-2}, respectively. Although the overpotential of $Ni_2P–WO_3$-30 is lower than that of $Ni_2P–WO_3$-60 at −10 mA cm^{-2}, the $Ni_2P–WO_3$-60 sample exhibits high performance when the current density increases. Moreover, the performance of $Ni_2P–WO_3$-60 was better than that of most previous studies (Table S3†). Moreover, the Tafel slope of $Ni_2P–WO_3$-60 is 55.9 mV dec^{-1} (Fig. 5b), which reveals that $Ni_2P–WO_3$-60 has a fast kinetic reaction process that follows the Volmer–Heyrovsky reaction mechanism.[29] $Ni_2P–WO_3$-60 also showed small charge transfer impedance (Fig. 5c). A long-term test was conducted for 36 h at −50 mA cm^{-2} in a 0.5 M H_2SO_4 electrolyte (Fig. 5d), along with a second test for 48 h in a 30% KOH electrolyte at 500 mA cm^{-2} (Fig. S8†). These results indicate that $Ni_2P–WO_3$-60 exhibited stable catalytic properties in both acidic and alkaline electrolytes.

The $Ni_2P–WO_3$-60 catalyst and RuO_2 were coupled into a two-electrode system and a high current density test was performed using characteristics analogous to a typical industrial process (Fig. 6a).[46] The $RuO_2^{(+)}\|Ni_2P–WO_3$-60$^{(-)}$ steady-state potential polarization curve is shown in Fig. 6b. Interestingly, when the cell voltage reaches 1.71 V, the current density of $RuO_2^{(+)}\|Ni_2P–WO_3$-60$^{(-)}$ is the same as that of the referenced system of $RuO_2^{(+)}\|Pt/C^{(-)}$. After that point, as the cell voltage increases, its performance is better than that of $RuO_2^{(+)}\|Pt/C^{(-)}$. Table S4† and Fig. 6c show the comparison of the previous reports with our HER catalysts. For the $RuO_2^{(+)}\|Ni_2P–WO_3$-60$^{(-)}$ system, a low cell voltage (∼1.73 V) can be achieved in 1.0 M KOH at 100 mA cm^{-2}. Finally, we conducted a stability test of the $RuO_2^{(+)}$-$\|Ni_2P–WO_3$-60$^{(-)}$ system under industrial conditions. It is worth noting that the stability test did not involve iR correction. As

shown in Fig. 6d, $RuO_2^{(+)}\|Ni_2P–WO_3\text{-}60^{(−)}$ worked continuously for 36 h at various high current densities (500–1000 mA cm^{-2}) with almost no apparent degradation.

As discussed above, the excellent HER activity of $Ni_2P–WO_3$ in acidic and alkaline electrolytes can be explained as follows: (i) the 3D self-supporting binder-free electrode synthesized by *in situ* electrodeposition can minimize the electrode resistance and promote electron/ion diffusion.[47] (ii) The porous morphology promotes proton transport and hydrogen adsorption, thereby effectively enhancing electron transfer. At the same time, $Ni_2P–WO_3$ has a higher electrochemically active surface area and more available catalytic active sites to improve the electrochemical performance.[48] (iii) The doping of amorphous tungsten enhances the synergistic effect of Ni and P in the Ni_2P structure, thereby effectively adjusting the electronic structure and minimizing the energy barrier in the electrolysis process.[49,50] (iv) Since tungsten oxide has high thermodynamic stability under acidic and alkaline solutions, the catalyst can work stably for a long time under harsh conditions.[51]

Conclusions

We constructed a series of nickel phosphides with different crystal structures by changing the W content. Among them, $Ni_2P–WO_3$-60 showed small overpotentials of 107 and 105 mV in 0.5 M H_2SO_4 and 1.0 M KOH electrolytes at −10 mA cm^{-2}, respectively, demonstrating excellent HER activity. In particular, it demonstrated considerably higher performance at high current density compared to the industry benchmark in a two-electrode system. The $Ni_2P–WO_3$-60 electrocatalyst exhibited high stability for over 36 h in a high current density gradient stability test under industrial alkaline conditions. The superior HER activity and excellent cycling stability are due to the unique 3D structure and the fact that amorphous WO_3 promotes electron transfer between P and Ni.

Conflicts of interest

The authors declare no competing financial interest.

Acknowledgements

Notes and references

1 C. Du, L. Yang, F. Yang, G. Cheng and W. Luo, *ACS Catal.*, 2017, **7**, 4131–4137.

2 Z. Jia, T. Yang, L. Sun, Y. Zhao, W. Li, J. Luan, F. Lyu, L.-C. Zhang, J. J. Kruzic, J.-J. Kai, J. C. Huang, J. Lu and C. T. Liu, *Adv. Mater.*, 2020, **32**, 2000385.

3 G. Wang, W. Chen, G. Chen, J. Huang, C. Song, D. Chen, Y. Du, C. Li and K. K. Ostrikov, *Nano Energy*, 2020, **71**, 104637.

4 L. Du, D. Feng, X. Xing, C. Wang, G. S. Armatas and D. Yang, *Chem. Eng. J.*, 2020, **400**, 125864.

5 J. Guo, B. Wang, D. Yang, Z. Wan, P. Yan, J. Tian, T. T. Isimjan and X. Yang, *Appl. Catal., B*, 2020, **265**, 118584.

6 Y. Li, X. Tan, H. Tan, H. Ren, S. Chen, W. Yang, S. C. Smith and C. Zhao, *Energy Environ. Sci.*, 2020, **13**, 1799–1807.

7 Y. Lei, Y. Wang, Y. Liu, C. Song, Q. Li, D. Wang and Y. Li, *Angew. Chem., Int. Ed.*, 2020, **59**, 20794–20812.

8 D. D. Tuan and K.-Y. A. Lin, *Chem. Eng. J.*, 2018, **351**, 48–55.

9 B. Wang, H. Huang, M. Huang, P. Yan, T. T. Isimjan and X. Yang, *Sci. China: Chem.*, 2020, **63**, 841–849.

10 H. Huang, Y. Zhao, Y. Bai, F. Li, Y. Zhang and Y. Chen, *Adv. Sci.*, 2020, **7**, 2000012.

11 Z. Chen, W. Gong, S. Cong, Z. Wang, G. Song, T. Pan, X. Tang, J. Chen, W. Lu and Z. Zhao, *Nano Energy*, 2020, **68**, 104335.

12 N. Mahmood, Y. Yao, J.-W. Zhang, L. Pan, X. Zhang and J.-J. Zou, *Adv. Sci.*, 2018, **5**, 1700464.

13 L. Pang, A. Barras, V. Mishyn, G. Sandu, S. Melinte, P. Subramanian, R. Boukherroub and S. Szunerits, *J. Mater. Chem. A*, 2020, **8**, 13980–13986.

14 J. Zhao, Z. Pu, H. Jin, Z. Zhang, J. Liu and S. Mu, *J. Catal.*, 2020, **383**, 244–253.

15 H. Zhao, Z. Li, X. Dai, M. Cui, F. Nie, X. Zhang, Z. Ren, Z. Yang, Y. Gan, X. Yin, Y. Wang and W. Song, *J. Mater. Chem. A*, 2020, **8**, 6732–6739.

16 M. Yang, Y. Jiang, M. Qu, Y. Qin, Y. Wang, W. Shen, R. He, W. Su and M. Li, *Appl. Catal., B*, 2020, **269**, 118803.

17 P. Liu and J. A. Rodriguez, *J. Am. Chem. Soc.*, 2005, **127**, 14871–14878.

18 Z.-J. Chen, G.-X. Cao, L.-Y. Gan, H. Dai, N. Xu, M.-J. Zang, H.-B. Dai, H. Wu and P. Wang, *ACS Catal.*, 2018, **8**, 8866–8872.

19 N. Danilovic, R. Subbaraman, D. Strmcnik, K.-C. Chang, A. P. Paulikas, V. R. Stamenkovic and N. M. Markovic, *Angew. Chem., Int. Ed.*, 2012, **51**, 12495–12498.

20 A. Królikowski and A. Wiecko, *Electrochim. Acta*, 2002, **47**, 2065–2069.

21 P. W. Menezes, A. Indra, C. Das, C. Walter, C. Göbel, V. Gutkin, D. Schmeiβer and M. Driess, *ACS Catal.*, 2017, **7**, 103–109.

22 R. B. Wexler, J. M. P. Martirez and A. M. Rappe, *J. Am. Chem. Soc.*, 2018, **140**, 4678–4683.

23 B. Owens-Baird, J. P. S. Sousa, Y. Ziouani, D. Y. Petrovykh, N. A. Zarkevich, D. D. Johnson, Y. V. Kolen'ko and K. Kovnir, *Chem. Sci.*, 2020, **11**, 5007–5016.

24 A. Martin, W. Kiarie, B. Chang and M. Thuo, *Angew. Chem., Int. Ed.*, 2020, **59**, 1.

25 F. Liu, L. Li, F. Mo, J. Chen, S. Deng and N. Xu, *Cryst. Growth Des.*, 2010, **10**, 5193–5199.

26 H.-L. Tsai, J. Heising, J. L. Schindler, C. R. Kannewurf and M. G. Kanatzidis, *Chem. Mater.*, 1997, **9**, 879–882.

27 Z. Jin, P. Li, X. Huang, G. Zeng, Y. Jin, B. Zheng and D. Xiao, *J. Mater. Chem. A*, 2014, **2**, 18593–18599.

28 X. Wang, X. Gan, T. Hu, K. Fujisawa, Y. Lei, Z. Lin, B. Xu, Z.-H. Huang, F. Kang, M. Terrones and R. Lv, *Adv. Mater.*, 2017, **29**, 1603617.

29 B. Wang, H. Huang, T. Sun, P. Yan, T. T. Isimjan, J. Tian and X. Yang, *J. Colloid Interface Sci.*, 2020, **567**, 339–346.

30 L.-A. Stern, L. Feng, F. Song and X. Hu, *Energy Environ. Sci.*, 2015, **8**, 2347–2351.

31 C. Liu, T. Gong, J. Zhang, X. Zheng, J. Mao, H. Liu, Y. Li and Q. Hao, *Appl. Catal., B*, 2020, **262**, 118245.

32 F. Cheng, L. Wang, H. Wang, C. Lei, B. Yang, Z. Li, Q. Zhang, L. Lei, S. Wang and Y. Hou, *Nano Energy*, 2020, **71**, 104621.

33 Z. Wan, Q. He, J. Chen, T. T. Isimjan, B. Wang and X. Yang, *Chin. J. Catal.*, 2020, **41**, 1745–1753.

34 R. Boppella, W. Yang, J. Tan, H.-C. Kwon, J. Park and J. Moon, *Appl. Catal., B*, 2019, **242**, 422–430.

35 J. Xie, B.-Q. Li, H.-J. Peng, Y.-W. Song, J.-X. Li, Z.-W. Zhang and Q. Zhang, *Angew. Chem., Int. Ed.*, 2019, **58**, 4963–4967.

36 D. Zhao, R. Zhao, S. Dong, X. Miao, Z. Zhang, C. Wang and L. Yin, *Energy Environ. Sci.*, 2019, **12**, 2422–2432.

37 T. Sun, J. Dong, Y. Huang, W. Ran, J. Chen and L. Xu, *J. Mater. Chem. A*, 2018, **6**, 12751–12758.

38 D. Zhang, J. Shi, Y. Qi, X. Wang, H. Wang, M. Li, S. Liu and C. Li, *Adv. Sci.*, 2018, **5**, 1801216.

39 J. Guo, M. Wang, X. Diao, Z. Zhang, G. Dong, H. Yu, F. Liu, H. Wang and J. Liu, *J. Phys. Chem. C*, 2018, **122**, 19037–19043.

40 D. Zhang, J. Shi, Y. Qi, X. Wang, H. Wang, M. Li, S. Liu and C. Li, *Adv. Sci.*, 2018, **5**, 1801216.

41 X. Zheng, H. Nie, Y. Zhan, X. Zhou, H. Duan and Z. Yang, *J. Mater. Chem. A*, 2020, **8**, 8273–8280.

42 C. Hegde, X. Sun, H. Ren, A. Huang, D. Liu, B. Li, R. Dangol, C. Liu, S. Li, H. Li and Q. Yan, *Nanoscale*, 2020, **12**, 8432–8442.

43 L. Najafi, S. Bellani, A. Castelli, M. P. Arciniegas, R. Brescia, R. Oropesa-Nuñez, B. Martín-García, M. Serri, F. Drago, L. Manna and F. Bonaccorso, *Chem. Mater.*, 2020, **32**, 2420–2429.

44 X. Yan, M. Gu, Y. Wang, L. Xu, Y. Tang and R. Wu, *Nano Res.*, 2020, **13**, 975–982.

45 Q. Cheng, C. Hu, G. Wang, Z. Zou, H. Yang and L. Dai, *J. Am. Chem. Soc.*, 2020, **14**, 5594–5601.

46 P. Yan, M. Huang, B. Wang, Z. Wan, M. Qian, H. Yan, T. T. Isimjan, J. Tian and X. Yang, *J. Energy Chem.*, 2020, **47**, 299–306.

47 K. Liang, S. Pakhira, Z. Yang, A. Nijamudheen, L. Ju, M. Wang, C. I. Aguirre-Velez, G. E. Sterbinsky, Y. Du, Z. Feng, J. L. Mendoza-Cortes and Y. Yang, *ACS Catal.*, 2019, **9**, 651–659.

48 R. Boppella, J. Tan, W. Yang and J. Moon, *Adv. Funct. Mater.*, 2019, **29**, 1807976.

49 Z. Peng, D. Jia, A. M. Al-Enizi, A. A. Elzatahry and G. Zheng, *Adv. Energy Mater.*, 2015, **5**, 1402031.

50 Y. Zheng, Y. Jiao, M. Jaroniec and S. Z. Qiao, *Angew. Chem., Int. Ed.*, 2015, **54**, 52–65.

51 T. Zheng, W. Sang, Z. He, Q. Wei, B. Chen, H. Li, C. Cao, R. Huang, X. Yan, B. Pan, S. Zhou and J. Zeng, *Nano Lett.*, 2017, **17**, 7968–7973.